# HIGH LIFT MECHANISM OF A 2D FLAPPING WING IN HOVERING FLIGHT

**Yunlong Zheng*, Qiulin Qu*, Peiqing Liu***
***Beihang University, Beijing, 100191, China**
**Keywords**: *flapping wing, high lift mechanism, unsteady flow*

## Abstract

*The aerodynamics of a 2D dragonfly wing in hover are investigated by solving the unsteady incompressible laminar flow N-S equations. A simplified elliptical wing with oscillating motion in an inclined stroke plane corresponding to Re =157 is studied. The correlation between the flow field and the aerodynamic forces is established through a new method, by which the high lift mechanism of flapping wing can be explained in detail.*

## 1 Introduction

Insects are the earliest appeared fliers which are capable of long-time hovering, fast forward flight and quick manoeuvers. Earlier studies have confirmed that insects use unsteady mechanisms to generate high lift enough to balance their own gravity [1]. Recently, due to the rapid development of Micro Air Vehicles (MAVs), the research on unsteady aerodynamics of flapping flight has received considerable attention.

So far, four main unsteady mechanisms associated with high lift have been identified, i.e. clap and fling, delayed stall associated with leading edge vortex (LEV), rapid pitch rotation and wake capture. The earliest discovered unsteady mechanism is the clap and fling by Weis-Fogh [2]. It was observed that before each downstroke, a chalcid wasp clapped two wings together and then quickly flung. During the flung motion, the air around each wing immediately acquired circulation in the correct direction to generate additional lift without Wagner effect, because one wing with its circulation acted as the starting vortex of the other wing. Although this form of motion is not employed by most insects, the discovery of the clap and fling mechanism pioneered the attention on unsteady mechanisms. By visualizing the flow field around the wing of a tethered hawkmoth and a hovering mechanical model, Ellington et al. [3] observed the delayed stall of LEV during the translation of each downstroke, which induced a negative pressure region hence enhancing the wing lift. Even the delayed stall mechanism is the most important among the four mechanisms and has been widely validated [4-9], the reason for the LEV attachment remains controversial. Ellington et al. [3], Berg and Ellington [10] considered the spanwise flow directed from the wing base to the wing tip drained energy from the vortex core which prevented the LEV from accumulating into a unstable large vortex. However, Birch and Dickinson [11] only found a much smaller spanwise flow about 2%-5% of the tip velocity at $Re \approx 150$, they suggested that the downward flow induced by the tip vortices limits the LEV growth. It is likely that the spanwise flow only occurs at sufficiently large *Re* as employed by hawkmoth. Besides, the delayed stall mechanism was also present in 2D hovering flight because the vortex shedding time scale was larger than the half flapping period of the wing as confirmed by Wang [9]. Dickinson et al. [4] measured the unsteady forces on a robotic fruit fly wing, in addition to the large lift during the translational portion of the half stroke, they also found the lift peaks at the beginning and the end of the half stroke. They attributed the lift peak at the beginning to the wake capture mechanism and that at the end to the rapid pitch rotation mechanism. In the subsequent research by Sun and Tang [5], the flow field of a model wing using the similar flapping motion and the same *Re* as Dickinson et al. [4] was simulated.

They confirmed that the lift peak at the end of the half stroke was due to the generation of strong vorticity layers over a short period which was consistent with Dickinson et al. [4]. However the lift peak at the beginning of the half stroke was explained by the rapid acceleration of the wing rather than the interaction between the wing and the wake left by the previous stoke. The follow-up researches [12-14] further proved that the wake capture mechanism had limited contribution to wing lift, and in some cases it even reduced lift.

The most significant characteristic of the 3D flow field is the presence of the spanwise flow. However, experiments on dynamically scaled wings [11] and free-flight visualizations [15] did not observe substantial spanwise flow which may related to the low $Re$. Sun and Lan [16] and Wang et al. [17] respectively confirmed that the aerodynamic forces predicted by 2D computation agreed well with the 3D computation and experiment results. Furthermore, considering the complexity and computational cost of the 3D modeling, it is reasonable to employ a 2D approach to study the flapping flight.

Although many researches have been done on insect flight, there was no other flow field details than vorticity and pressure contours during the analysis. Researchers generally corresponded the vortex structures to the pressure contours, then the aerodynamic forces were immediately explained by the spatial pressure distributions. The authors think the current analytical method can be further refined. For this reason, a new analytical method has been proposed which will be introduced in detail.

Up to now, the correlation between the flow field structure and the aerodynamic force is not clear, there is a lack of in-depth study. In view of the above deficiencies, a 2D elliptical wing mimicking dragonfly hovering flight is simulated. Although the current physical model has many limitations, it is still suitable for explaining the aerodynamic mechanisms and providing the basis for the subsequent 3D studies.

## 2 Physical Model and Numerical Method

### 2.1 Physical Model

Among the different flying modes, hovering poses the most challenge to insects partly due to the complex interaction between the flapping wing and the wakes that generated during the preceding strokes [18, 19]. Therefore, in the present study, a 2D wing motion based on the dragonfly hovering data proposed by Wang [9] was adopted. The model wing is elliptical with chord length $c$ equals to $1cm$ and minor to major axis ratio 0.25, furthermore it is divided into windward and leeward along major axis. The wing begins to flap in the quiescent flow, and the wing kinematics are given by：

$$A(t)=\frac{A_0}{2}\left[\cos\left(2\pi t/T\right)+1\right] \qquad (1)$$

$$\alpha(t)=\frac{\pi}{4}-\frac{\pi}{4}\sin\left(2\pi t/T\right) \qquad (2)$$

where $A(t)$ is the translational displacement of the wing centroid along the stroke plane, $\alpha(t)$ is the angle of attack (AoA), $A_0$ is the translational amplitude which equals to $2.5cm$ and $T$ is the flapping period which equals to $0.025s$. The wing moves along an inclined plane (called the stroke plane) and the angle between the plane and the horizontal is $\beta$ which is selected as $60^\circ$ in the current paper based on the observation of Wakeling and Ellington [20] and Norberg [21]. In addition, both Sun and Lan [16] and Wang [22] confirmed that dragonfly uses drag to support its weight with the inclined stroke plane. Sketch of the coordinate system and the wing motion are shown in Fig. 1. The $Re=Uc/\upsilon=A_0\pi c/T\upsilon$ under the current condition is 157, where the reference speed $U=A_0\pi/T$ is the maximum translational velocity and $\upsilon=2.0cm^2/s$ is the kinematic viscosity. The above values of parameters and $Re$ are typical employed in dragonfly flight [20, 21].

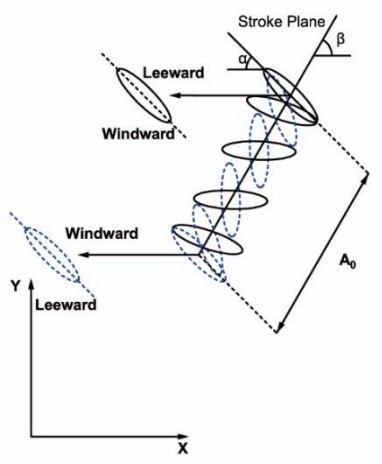


**Fig. 1.** Sketch of the coordinate system and the wing motion.

## 2.2 Numerical Method

We employ the commercial computational fluid dynamics (CFD) software ANSYS Fluent Version 16.0 that adopts finite volume method (FVM) to solve the unsteady incompressible laminar Navier-Stokes equations to simulate the unsteady flow field of the hovering 2D flapping wing. The wing motion is implemented through a user defined function (UDF) and is simulated by the dynamic mesh method.

## 2.3 Validation of Numerical Method

We simulate the same condition as Wang [9], the force coefficients change with non-dimensional time $t^*$ (which equals to $t/T$) are compared in Fig. 2. The force history curves show perfect periodicity after the 5th period, thus the aerodynamic forces and flow structures in the 6th period are used in the following analysis. As can be seen from Fig. 2 that the present results agree well with the previous which indicates the current numerical method is applicable.

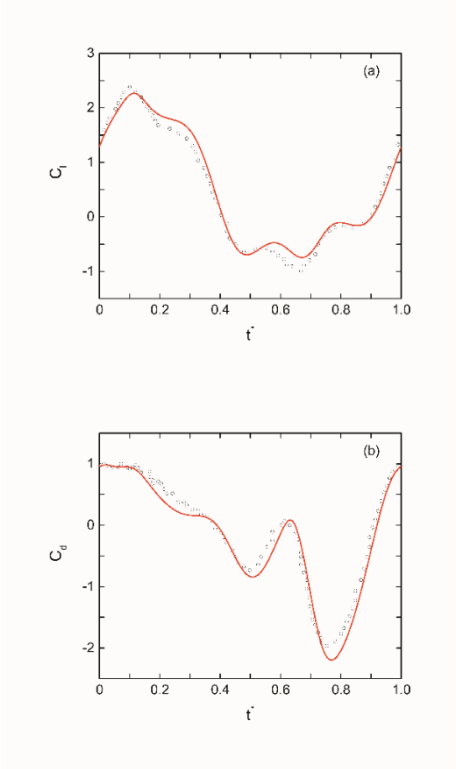


**Fig. 2.** Comparison of the (a) lift and (b) drag coefficient curves between the present result and from Ref. [9]: —, present; ∘ Ref.

## 3 Results and Discussion

### 3.1 Analysis Road Map

In view of the insufficient of the previous analytical method, a new method is proposed as exhibited in Fig. 3 which will be described in detail: due to both the translational and rotational motions of the wing and the vortices induce fluid flows which will change the flow field prominently. In order to facilitate the analysis, the flow is classified into vertical surface flow and parallel surface flow according to the direction. The vertical flow directly impinges on the wing surface to form a positive pressure zone, and the parallel flow generates boundary layer on the wing surface due to the wall shear, when the boundary layer accumulates to a certain extent, it will shed and form a concentrated vortex, meanwhile the concentrated vortex induced flow again induces a secondary vortex or fluid impact on the wing surface. The above three types of vortex all generate negative pressure. So far, the correspondence between the flow field and the

pressure coefficient distribution on the wing surface can be obtained. It is worth noting that with $Re$ in our case, the aerodynamic forces are dominated by the dynamic pressure rather than by the viscous force as confirmed by Dickinson et al. [4], so we only focus on the dynamic pressure which is perpendicular to the wing surface. Furthermore, by integrating the pressure coefficient respectively along the major axis and the minor axis to obtain $C_a$ and $C_b$. Among them, $C_a$ is simply related to the vortex-induced negative pressure, while $C_b$ is mainly related to the positive pressure formed by the fluid impact and the negative pressure induced by vortices. Hereafter, by combining $C_a$ and $C_b$ with the AoA, the resultant aerodynamic force coefficient $C_r$ and its unit component in the lift direction $\sin\theta$ (where $\theta$ is the angle between the positive $x$ axis and the $C_r$ which ranges from $0^\circ$ to $360^\circ$) can be obtained, the two parameters together determine the lift coefficient $C_l$. Ultimately, the correlation between the flow field and the lift coefficient is established.

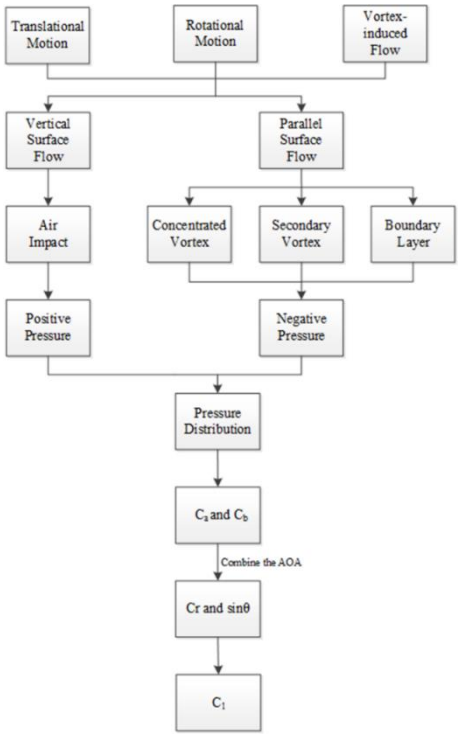


**Fig. 3.** Analysis road map.

## 3.2 Aerodynamic Force

In the first place, we focus on the variation of the aerodynamic forces. Fig. 4 exhibits the lift and drag coefficient curves in a complete cycle.

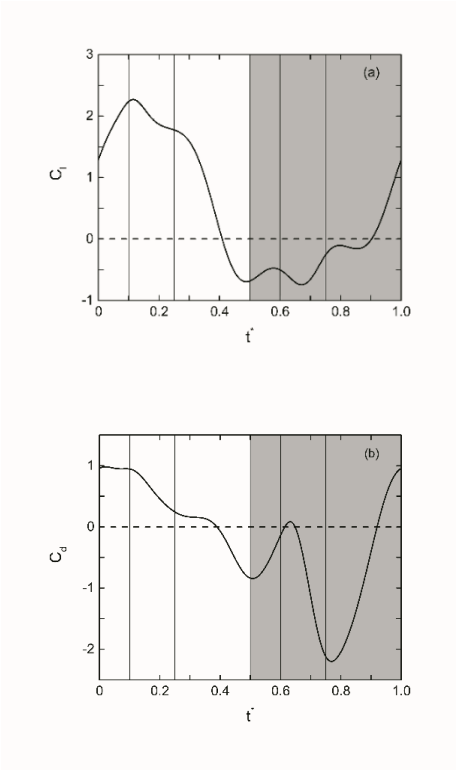


**Fig. 4.** (a) Lift and (b) drag coefficient curves in a complete cycle, white background represents the downstroke and gray background represents the upstroke, vertical bars represent the typical moments.

As mentioned before, by integrating the pressure coefficient respectively along the major and the minor axis to obtain $C_a$ and $C_b$ as shown in Fig. 5. The positive direction of $C_a$ is from the trailing edge to the leading edge and the positive direction of $C_b$ is from the initial windward surface to the leeward surface. It can be seen from the figure that the absolute value of $C_b$ is much greater than $C_a$, which indicates that $C_b$ provides most of the aerodynamic force. Simultaneously considering the flow field and the aerodynamic force change, six typical moments are chosen for analysis in a cycle. In order to describe the flapping motion in detail, the flow field and aerodynamic force during six time periods divided by six moments will be analyzed.

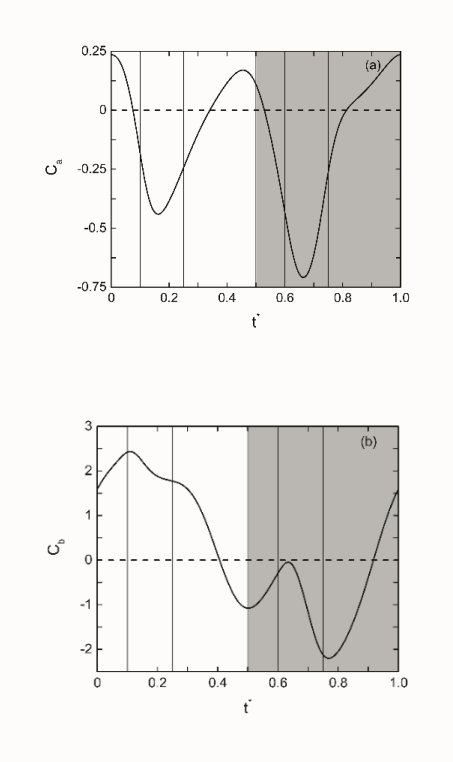


**Fig. 5.** Resultant force coefficient along (a) major axis $C_a$ and (b) minor axis $C_b$.

## 3.3 Flow Field

The translational velocity $u$ and the rotational angular velocity $\omega$ are given in Fig. 6 to better illustrate the movement.

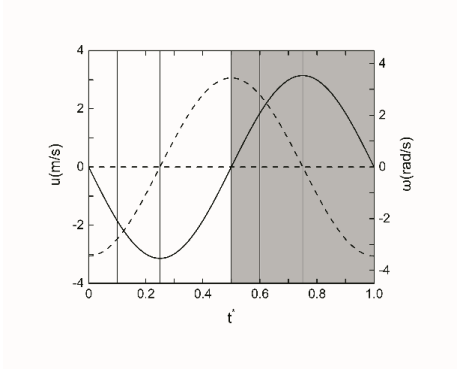


**Fig. 6.** Translational velocity $u$ and rotational velocity $\omega$ in a cycle: — $u(t)$ ; --- $\omega(t)$ .

Fig. 7 respectively shows the vorticity contour with streamlines (taking the wing centroid as the reference point), the pressure coefficient distribution on the wing surface and the schematic diagram of force coefficients and wing motion during $t^* = 0 - 0.1$ . In order to distinguish between different vortices, the vortices are named in a uniform way, namely LEV/TEV-0/1/2-Down/Up-1/2. Where LEV and TEV respectively represent leading edge vortex and trailing edge vortex; 0/1/2 denotes the cycle of the vortex generation, furthermore, 0 represents the current cycle, 1 represents the previous cycle and 2 represents the cycle before the previous; Down/Up respectively represent the vortex is generated in downstroke or upstroke; 1/2 respectively indicate the order of the vortices when vortex splits. That is, 1 represents the main vortex and 2 represents the newly split vortex.

(a)

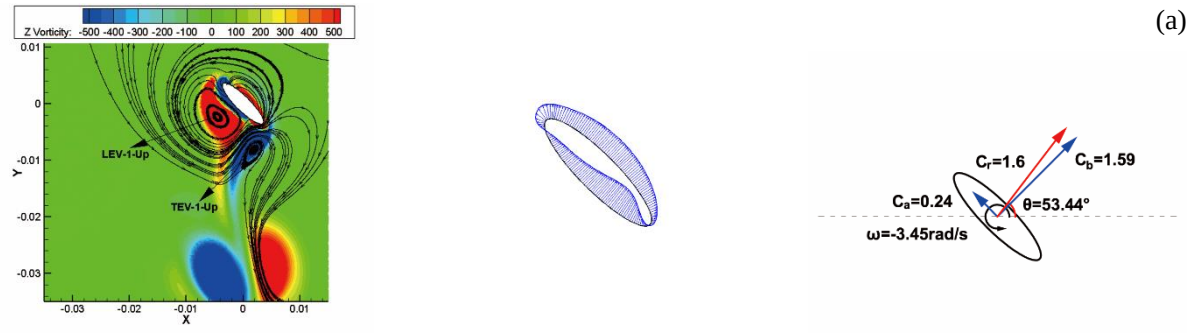

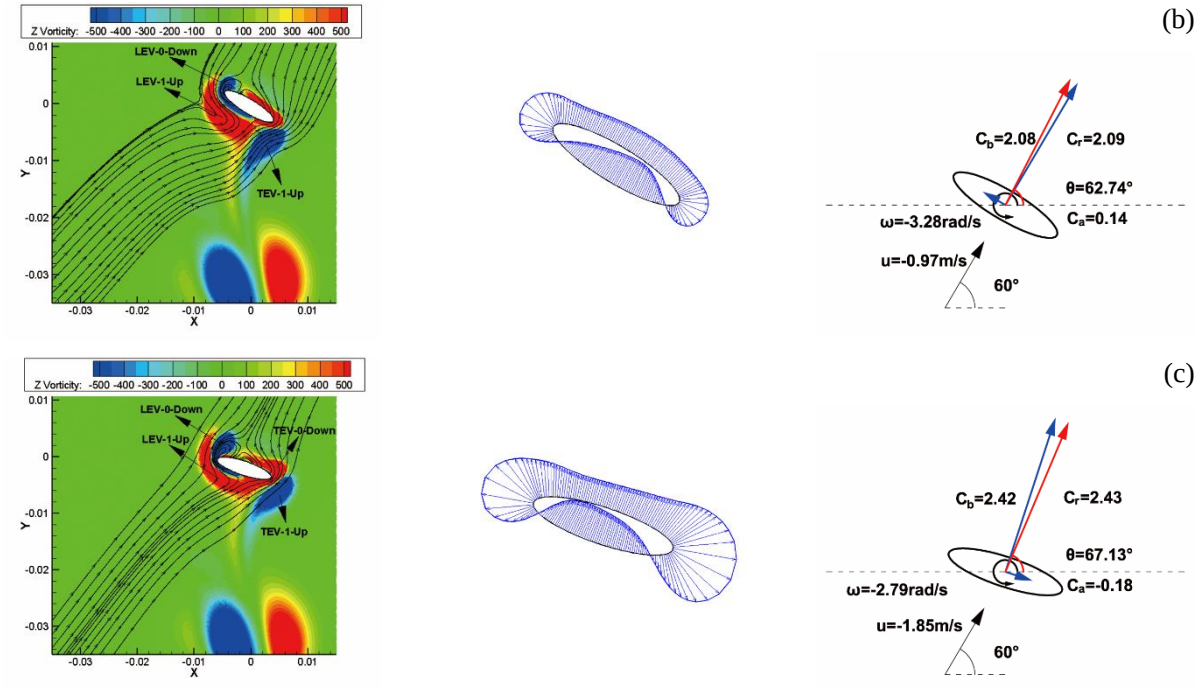


**Fig. 7.** Vorticity contour with streamlines, pressure coefficient distribution and the schematic diagram of force coefficients and wing motion respectively at (a) $t^* = 0$, (b) $t^* = 0.05$ and (c) $t^* = 0.1$.

At $t^* = 0$, the shed double vortex LEV-1-Up and TEV-1-Up is located on the leeward side of the wing and the wake capture mechanism takes effect: the double vortex induces vertical flow to impinge on the leeward surface forming a positive pressure zone which is also confirmed by Dickinson et al. [4]. It can be seen from the pressure coefficient distributions that the pressure on the leeward surface of the wing is positive, that is, under the current condition, the wake capture mechanism has the positive effect of increasing wing lift.

During $t^* = 0 - 0.1$, Fig. 6 indicates $u$ increases monotonically from zero and $\omega$ decreases monotonically from the maximum, the translational and rotational motions of the wing together with the vortex-induced flow determine the flow field. The vorticity contours imply that LEV-1-Up and TEV-1-Up shed in the last stroke gradually dissipate and their induction on flow impinging on the windward surface is weakened. However, due to $u$ increases, the velocity of the inflow increases, therefore the value of positive pressure zone on windward surface formed by the air impact still increases. Eventually $C_b$ monotonically increases to the peak as shown in Fig. 5 (b). The wing motion causes the new LEV-0-Down and TEV-0-Down to generate. As the resultant velocity of the fluid near the leading edge (translational speed minus rotational speed) is less than that near the trailing edge (translational speed plus rotational speed), the intensity of LEV-0-Down is significantly weaker than TEV-0-Down, hence the negative pressure on the leading edge is smaller than the trailing edge, resulting in monotonic $C_a$ decrease as displayed in Fig. 5 (a).

Next, we further explore how the flow field change alter the wing lift. For this purpose,

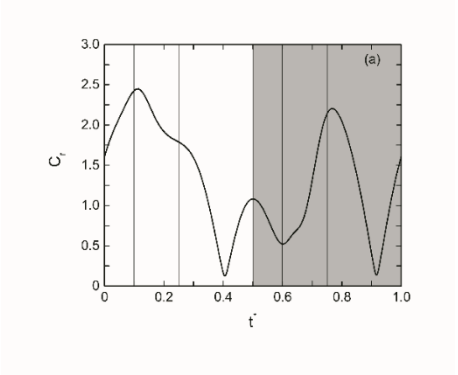

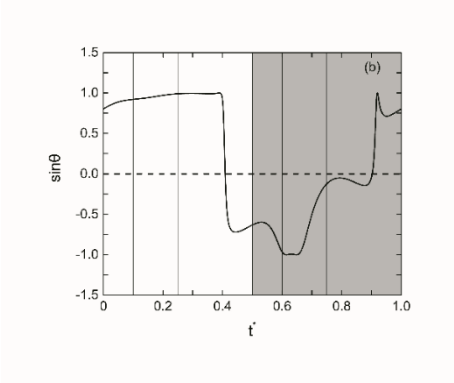


**Fig. 8** exhibits the resultant aerodynamic force coefficient $C_r$ and its unit component in the lift direction $\sin\theta$. According to the figure, during the current time period, $C_r$ increases monotonically to the peak, and $\sin\theta$ also increases monotonically. The $C_r$ increment and its component increment in the lift direction together lead $C_l$ to increase monotonically to the peak as shown in Fig. 4 (a).

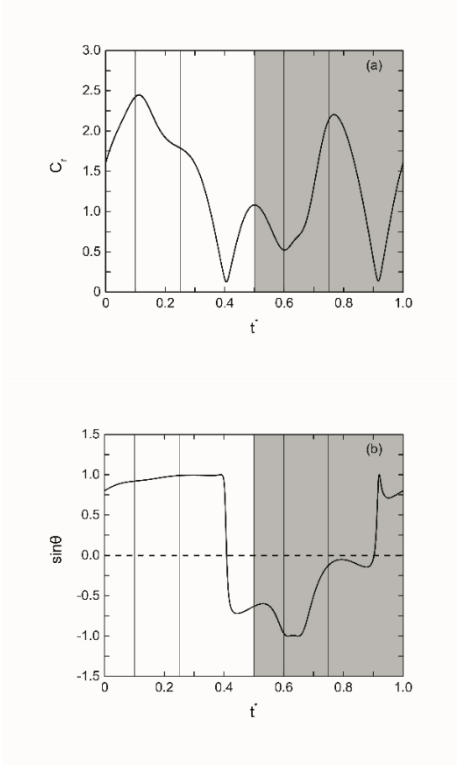


**Fig. 8.** (a) Resultant aerodynamic force coefficient $C_r$ and (b) its unit component in the lift direction $\sin\theta$.

In the next period of $t^* = 0.1 - 0.25$, $u$ increases monotonically to the maximum and $\omega$ decreases monotonically to zero, the flow field is mainly determined by the wing translation and the vortex-induced flow. Vorticity contours, pressure distributions and schematic diagrams are shown in Fig. 9. As can be seen from the streamlines that the impact position of the inflow on the windward surface gradually moves toward the leading edge. Meanwhile, due to the decrease of $\omega$, the resultant velocity of the inflow near the leading edge remains unchanged, even $u$ increases. As a result, the peak of the positive pressure is basically the same in the current time period. In addition, the inflow near the trailing edge of the windward surface is mainly parallel which generates a strong boundary layer and then induces negative pressure, resulting in a decrease in the range of positive pressure zone on the windward surface, therefore $C_b$ decreases monotonously. Besides, TEV-0-Down gradually enhances and sheds which causes the negative pressure on the trailing edge decreases. LEV-0-Down remains attached, which indicates that there is still a delayed stall mechanism in 2D case. Wang [9] believed this phenomenon is due to the vortex shedding time scale is larger than the half flapping period. Consequently, the induced negative pressure on the leading edge remains basically unchanged.

During this time period, $C_r$ monotonically decreases and $\sin\theta$ slightly increases, thus the decrease of $C_l$ is caused by $C_r$ alone.

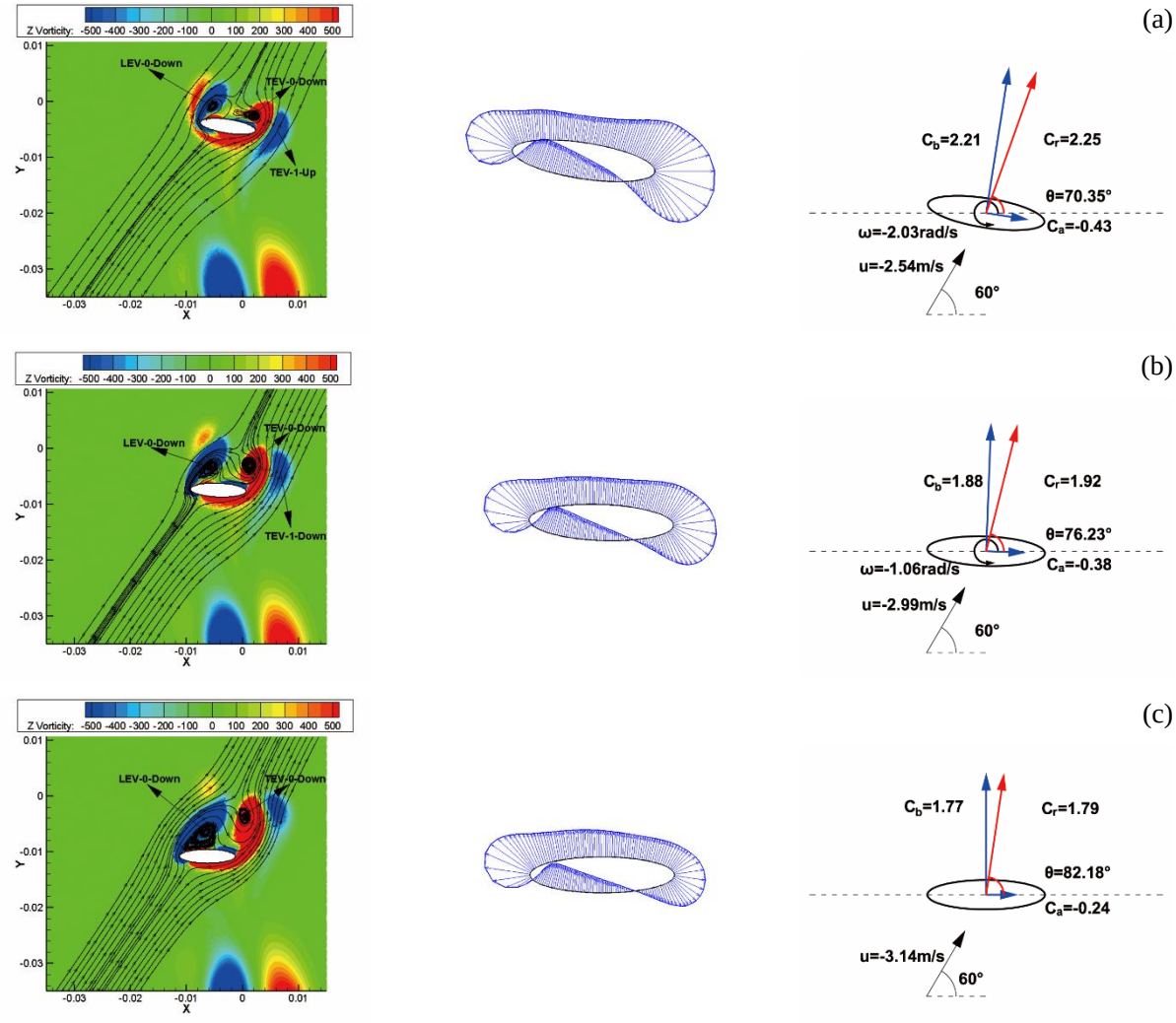


**Fig. 9.** Vorticity contour with streamlines, pressure coefficient distribution and the schematic diagram of force coefficients and wing motion respectively at (a) $t^* = 0.15$, (b) $t^* = 0.2$ and (c) $t^* = 0.25$.

In the period of $t^* = 0.25 - 0.5$, $u$ decreases monotonically to zero and $\omega$ increases monotonically to the maximum, initially the flow field is mainly determined by the wing translation and the vortex-induced flow, then the wing rotation instead of translation together with vortex-induced flow determine the flow field. Vorticity contours, pressure distributions and schematic diagrams are shown in Fig. 10. In the early stage $t^* = 0.25 - 0.4$, the decrease of $u$ leads to reduced inflow rate, hence the positive pressure on the windward surface dramatically decreases which results in a significant reduction in $C_b$. TEV-0-Down is further away from the wing and LEV-0-Down begins to shed, so the negative pressure on the leading and trailing edges decreases. In the end stage $t^* = 0.4 - 0.5$, the wing rotation dominates the wing translation. As can be seen from the streamlines, the direction of the flow near the windward surface is changed from the trailing edge to the leading edge due to wing rotation, and a strong boundary layer is generated which induces a negative pressure zone. LEV-0-Down induces a positive secondary vortex at the front of the leeward surface meanwhile induces a negative secondary vortex at the rear of the leeward surface. Besides, LEV-0-Down induces the flow to impinge on the leeward surface and generates a positive pressure zone. The above reasons together lead to a significant reduction in $C_b$. It is worth noting that at the end of the downstroke, the strong vorticity layers on the wing surface are not only related to the rapid rotation which was confirmed by Sun and Tang

[5], the shed LEV-0-Down also indirectly affects the vorticity layer generations.

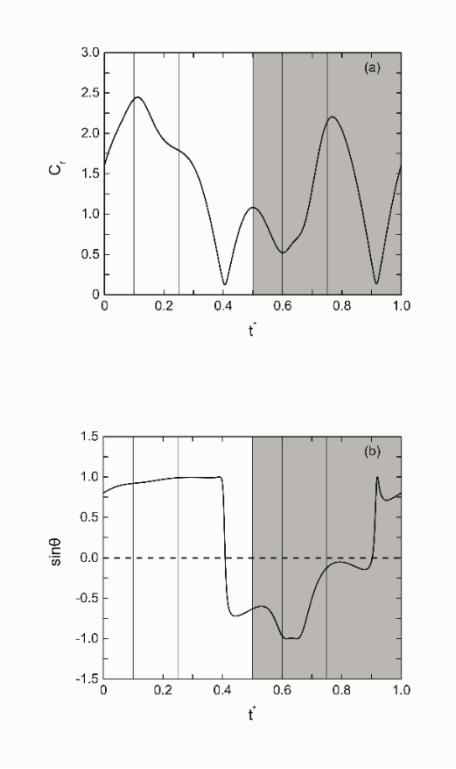


**Fig. 8** indicates that in the early time period of $t^* = 0.25 - 0.4$, $C_r$ decreases monotonically to the minimum, $\sin\theta$ is almost unchanged, the monotonous decrease of $C_l$ is caused by $C_r$ alone; in the later period of $t^* = 0.4 - 0.5$, $C_r$ increases monotonically, $|\sin\theta|$ slightly decreases, therefore the monotonous decrease of $C_l$ is caused by $C_r$ alone. That is, under the current form of motion, the rapid pitch rotation mechanism has the effect of reducing lift.

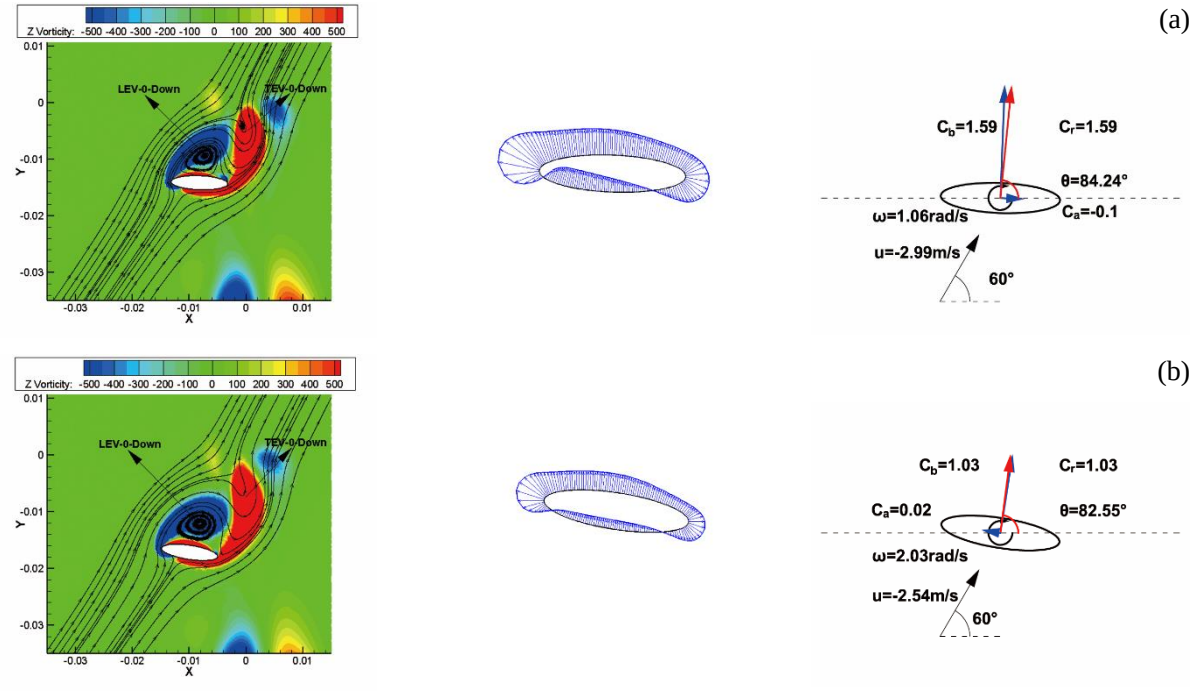

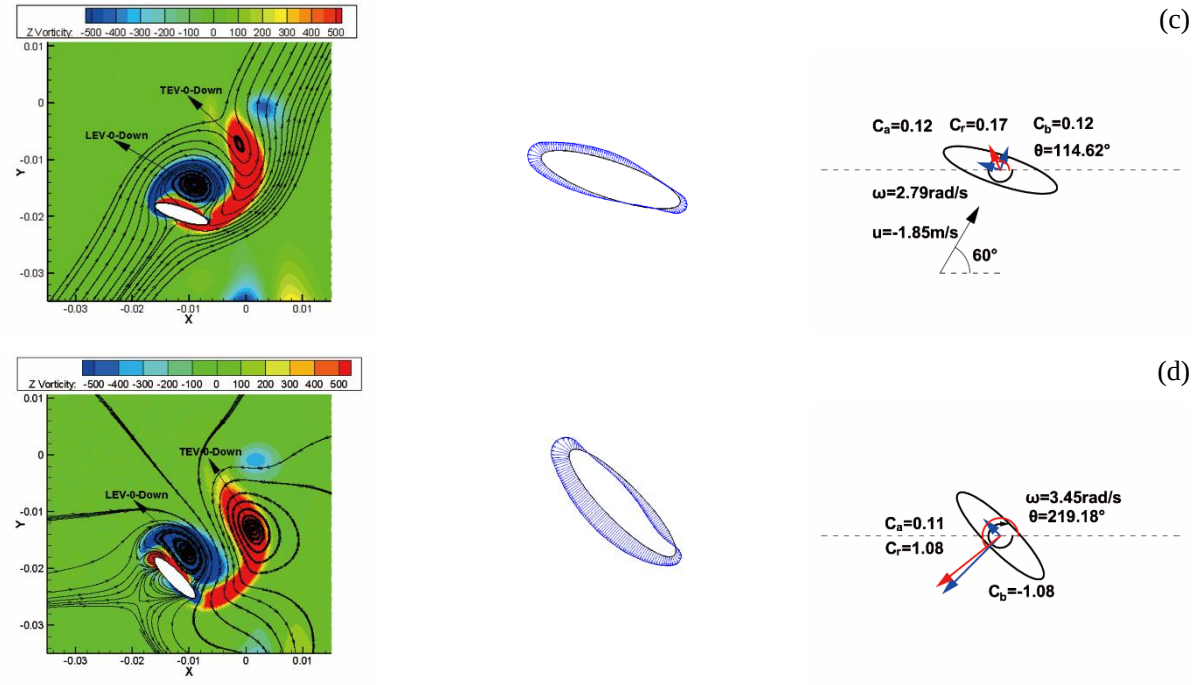


**Fig. 10**. Vorticity contour with streamlines, pressure coefficient distribution and the schematic diagram of force coefficients and wing motion respectively at (a) $t^* = 0.3$, (b) $t^* = 0.35$, (c) $t^* = 0.4$, (d) $t^* = 0.5$.

Next, the wing converts from downstroke to upstroke. In the time period of $t^* = 0.5 - 0.75$, the lift curve slightly oscillates. For the sake of brevity, no detailed analysis is performed.

In the last time period of $t^* = 0.75 - 1$, $u$ monotonically reduces to zero and $\omega$ monotonically increases to the maximum, the wing rotation and the vortex-induced flow begin to determine the flow field. Vorticity contours, pressure distributions and schematic diagrams are shown in Fig. 11. It can be seen from the figure that LEV-0-Up begins to shed and forms a vortex pair with the shed TEV-0-Up, this vortex pair initially induces negative pressure on the leeward surface due to it is close to the wing. As the vortex pair gradually sheds, it begins to mainly induce the fluid to impinge on the leeward surface. The flow on the windward side changes from vertical to parallel to the wing surface which mainly generates boundary layers and then induces negative pressure. In view of the above reasons, $C_b$ monotonically increases.

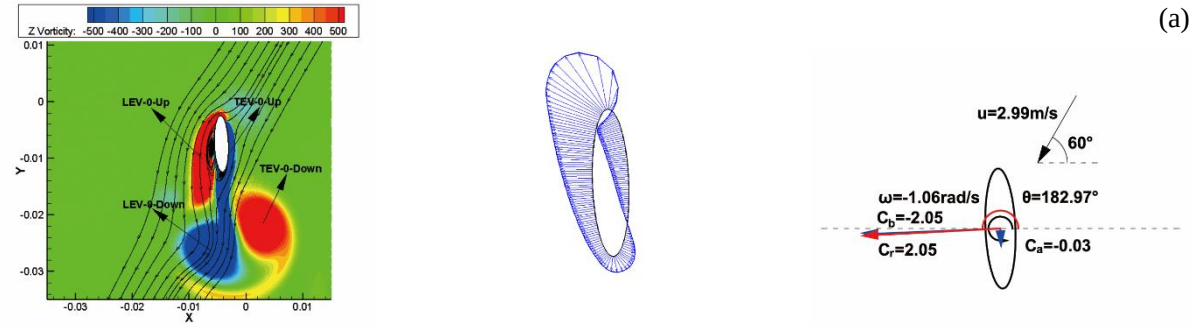

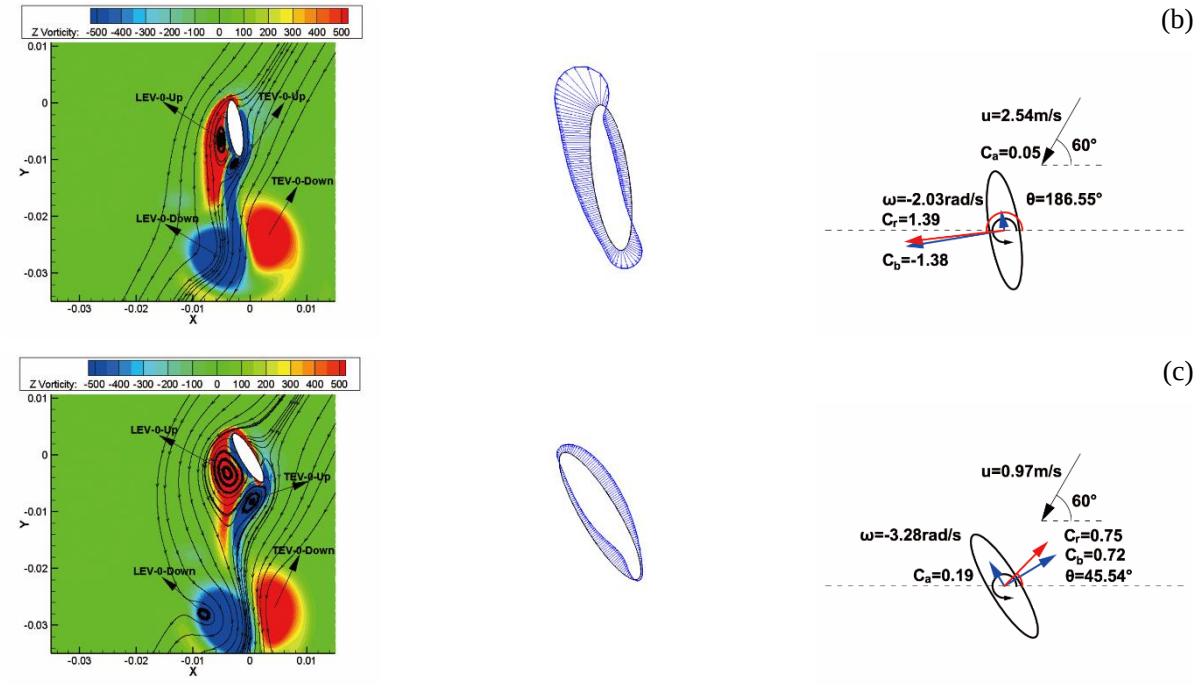


**Fig. 11.** Vorticity contour with streamlines, pressure coefficient distribution and the schematic diagram of force coefficients and wing motion respectively at (a) $t^* = 0.8$, (b) $t^* = 0.85$, (c) $t^* = 0.95$.

## 4 Conclusions

The correlation between the flow field and the aerodynamic forces is established through a new method which considers the flow caused by wing motion and vortex-induced simultaneously. In addition, three kinds of widely recognized high lift mechanisms are verified, the result is as follows: under the current wing motion, both the wake capture and delayed stall mechanisms have the effect of increasing lift; while the rapid pitch rotation mechanism has negative impact on the lift generation. The results of the research are helpful to understand the mechanisms of insect hovering flight. However, many deficiencies still exist that need to be perfected. For example, under the real situation, the dragonfly has two pairs of wings and the wing motion is 3D, so the associated fore and hind wings aerodynamic interference and 3D effect will be further considered in the subsequent studies.

## References

[1] Ellington CP. The aerodynamics of hovering insect flight. Ⅰ. the quasi-steady analysis. *Phil Trans R Soc Lond B* 1984; 305: 1-15.

[2] Weis-Fogh T. Quick estimates of flight fitness in hovering animals, including novel mechanisms for lift production. *J Exp Biol* 1973; 59: 169-230.

[3] Ellington CP, Berg CVD, Willmott AP, et al. Leading-edge vortices in insect flight. *Nature* 1996; 384: 626-630.

[4] Dickinson MH, Lehmann FO and Sane SP. Wing rotation and the aerodynamic basis of insect flight. *Science* 1999; 284: 1954-1960.

[5] Sun M and Tang J. Unsteady aerodynamic force generation by a model fruit fly wing in flapping motion. *J Exp Biol* 2002; 205: 55-70.

[6] Dickinson MH. Haltere-mediated equilibrium reflexes of the fruit fly, Drosophila melanogaster. *Phil Trans R Soc Lond B* 1999; 354: 903-916.

[7] Usherwood JR and Ellington CP. The aerodynamics of revolving wings I. Model hawkmoth wings. *J Exp Biol* 2002; 205: 1547-1564.

[8] Usherwood JR and Ellington CP. The aerodynamics of revolving wings II. Propeller force coefficients from mayfly to quail. *J Exp Biol* 2002; 205: 1565-1576.

[9] Wang ZJ. Two dimensional mechanism for insect hovering. *Phys Rev Lett* 2000; 85: 2216-2219.

[10] Berg CVD and Ellington CP. The three–dimensional leading–edge vortex of a 'hovering' model hawkmoth. *Phil Trans R Soc Lond B* 1997; 352: 329-340.

[11] Birch JM and Dickinson MH. Spanwise flow and the attachment of the leading-edge vortex on insect wings. *Nature* 2001; 412: 729-733.

[12] Birch JM and Dickinson MH. The influence of wing-wake interactions on the production of aerodynamic forces in flapping flight. *J Expl Biol* 2003; 206: 2257-2272.
[13] Wu JH and Sun M. The influence of the wake of a flapping wing on the production of aerodynamic forces. *Acta Mech Sinica-prc* 2005; 21: 411-418.
[14] Lu H, Lua KB, Lee YJ, et al. Ground effect on the aerodynamics of three-dimensional hovering wings. *Bioinspir Biomim* 2016; 11: 066003.
[15] Srygley RB and Thomas ALR. Unconventional lift-generating mechanisms in free-flying butterflies. *Nature* 2002; 420: 660-664.
[16] Sum M and Lan SL. A computational study of the aerodynamic forces and power requirements of dragonfly (Aeschna Juncea) hovering. *J Exp Biol* 2004; 207: 1887-1901.
[17] Wang ZJ, Birch JM and Dickinson MH. Unsteady forces and flows in low Reynolds number hovering flight: two-dimensional computations vs robotic wing experiments. *J Exp Biol* 2004; 207: 449-460.
[18] Lua KB, Lim TT and Yeo KS. Aerodynamic forces and flow fields of a two-dimensional hovering wing. *Exp Fluids* 2008; 45: 1067-1071.
[19] Lua KB, Lim TT and Yeo KS. Effect of wing–wake interaction on aerodynamic force generation on a 2D flapping wing. *Exp Fluids* 2011; 51: 177-195.
[20] Wakeling JM and Ellington CP. Dragonfly flight. II. Velocities, accelerations and kinematics of flapping flight. *J Exp Biol* 1997; 200: 557-582.
[21] Norberg RA. *Hovering flight of the dragonfly Aeschna juncea L., kinematics and aerodynamics.* New York: Plrnum Press: Springer US, 1975, p.763-781.
[22] Wang ZJ. The role of drag in insect hovering. *J Exp Biol* 2004; 207: 4147-4155.

## Copyright Statement



## Contact Author Email Address

qql@buaa.edu.cn